CHEMISTRY OF MATERIALS

pubs.acs.org/cm

Article

Two Distinct Stages of Structural Modification of ZIF-L MOF under Electron-Beam Irradiation

Supriya Ghosh, Hwanhui Yun, Prashant Kumar, Sabrina Conrad, Michael Tsapatsis, and K. Andre Mkhoyan*

Cite This: *Chem. Mater.* 2021, 33, 5681−5689

Read Online

ACCESS | Metrics & More | Article Recommendations | Supporting Information

ABSTRACT: Metal−organic frameworks (MOFs) are gaining more prominence as low-dielectric materials for applications in electronic devices and sensors using top−down electron-beam patterning. Using a combination of electron diffraction and electron energy-loss spectroscopy (EELS) in a transmission electron microscope, the details of structural modification of ZIF-L MOF under electron-beam irradiation were identified. It was found that the modification of ZIF-L under the electron beam happens in two distinct stages. In addition to the collapse of the original ZIF-L porous framework and loss of crystallinity occurring at the initial low-dose stage, it was observed that the disordered ZIF-L then undergoes a second stage of changes, where the molecular structure of the linker starts to breakdown. Further, it was observed that the degradation of the linker molecules in the second stage of the ZIF-L modification has a considerable impact on its dielectric function, shifting energies of the electronic transitions.

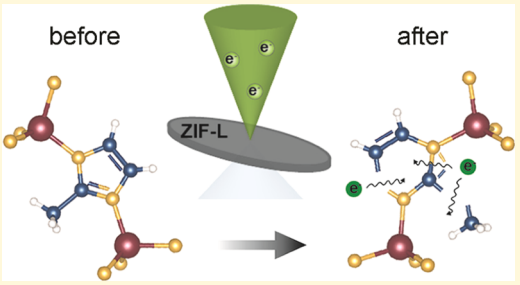

INTRODUCTION

Metal−organic frameworks[1] (MOFs) are an emerging class of synthesized materials with considerable promise owing to the flexibility in the choice of metal atoms and organic linkers. The porous structure of MOFs makes them very attractive materials for applications in gas storage,[2,3] gas separations,[4,5] and catalysis.[6] One of the most commonly studied subgroups of MOFs is zeolitic imidazole frameworks[7] (ZIFs), where typically Zn metal atoms are tetrahedrally coordinated to imidazole molecules resembling the Si−O−Si linkages present in zeolites.[8] In addition to crystalline ZIFs, it has been shown that amorphous ZIFs,[9−11] which can be made from their crystalline frameworks through ball milling,[12] heating,[13] pressurizing,[14] electrical discharge,[15] and X-ray[16] and electron-beam irradiations,[17−19] can also be very attractive materials for optical devices and sensors due to their low-dielectric constants.[20−23]

For large-scale device applications of amorphous and crystalline ZIFs, high-precision patterning is essential. It has been demonstrated that patterning of amorphous and crystalline ZIFs is achievable by an electron or X-ray beam.[16−19] However, to improve the control of electron-beam patterning of ZIFs, an in-depth study of the structural and chemical changes under electron-beam irradiation is needed. While there are numerous reports in the literature discussing electron-beam-induced structural changes in inorganic crystalline materials through distinct and clearly identifiable radiolitic and knock-on mechanisms,[24,25] the reports on MOFs are very limited.[26−30]

In this work, an in-depth study of the transition of a ZIF MOF from an ordered crystalline state to a disordered "amorphous" state under continuous electron-beam irradiation is carried out using dose-controlled transmission electron microscopy (TEM) combined with electron energy-loss spectroscopy (EELS). To identify the internal structural changes occurring in the linker molecules, additional measurements were conducted on the free-standing linker molecules. A combination of bright-field (BF) TEM and high-angle annular dark-field scanning transmission electron microscopy (HAADF-STEM) imaging, electron diffraction, and EELS is employed to reveal the morphological, structural, and electronic structure changes in the MOF as a function of the irradiating electron dose. Together, these techniques provide new insight into the distinct stages of structural modification of the crystalline ZIF MOF.

RESULTS AND DISCUSSIONS

For this study, a ZIF MOF known as ZIF-L was selected. In this framework, Zn metal atoms are linked by 2-methylimidazole (2-mIm) molecules, as shown in Figure 1a. ZIF-L arranges into an orthorhombic lattice with lattice constants of

Received: April 17, 2021
Revised: May 27, 2021
Published: June 8, 2021

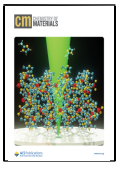

https://doi.org/10.1021/acs.chemmater.1c01332
Chem. Mater. 2021, 33, 5681−5689

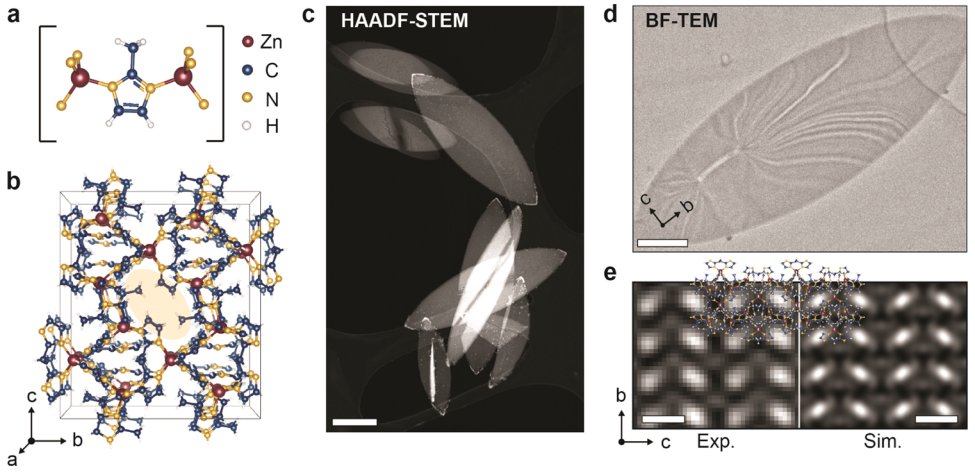

Figure 1. Structure and morphology of the ZIF-L MOF. (a) Model of the two Zn atoms linked together with a 2-mIm molecule, which is the building block for ZIF-L MOF. (b) Unit cell of ZIF-L viewed along the *a*-direction with the large central pore highlighted in yellow. (c) Low-magnification HAADF-STEM image of ZIF-L particles showing leaf-like morphology. The scale bar is 2 μm. (d) BF-TEM image showing bend contours in a single ZIF-L particle. The scale bar is 1 μm. (e) Wiener-filtered and cross-correlated high-resolution TEM image of the ZIF-L showing the alternating arrangement of the pores, along with the simulated TEM image. The atomic model is overlaid to highlight the pore arrangement. The scale bar is 1 nm.

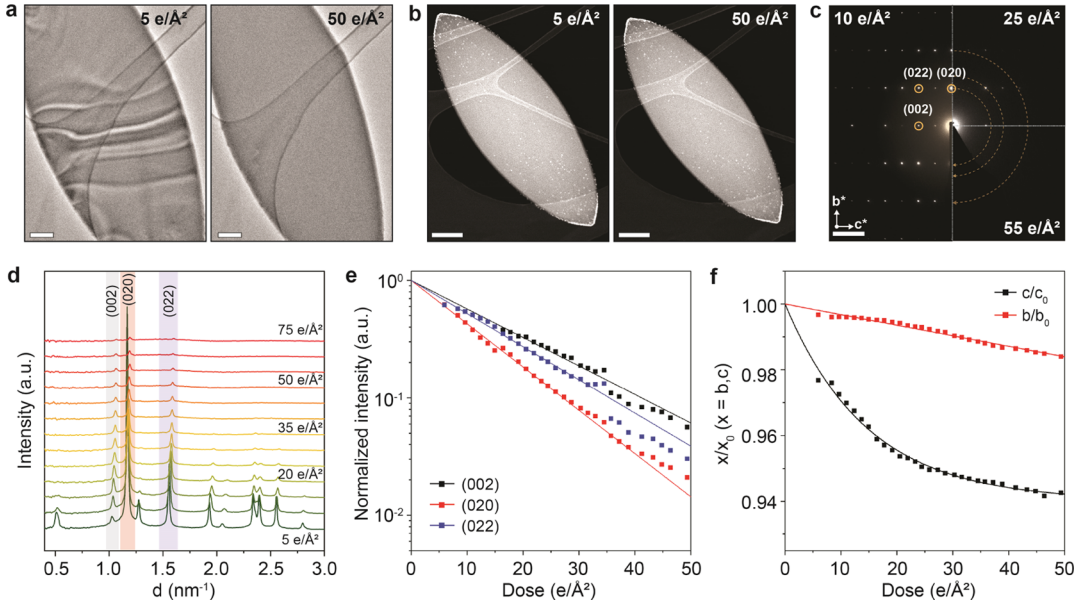

Figure 2. Dose-dependent electron diffraction of ZIF-L MOF. (a) BF-TEM images of ZIF-L MOF before and after exposure to the 50 e/Å^2 electron beam showing loss of diffraction contrast. The scale bar is 500 nm. (b) HAADF-STEM images of the ZIF-L MOF particle before and after exposure to the 50 e/Å^2 electron beam. The scale bar is 1 μm. (c) Electron diffraction from ZIF-L along the [100] zone axis. Left panel shows all higher-order reflections present at a very low dose. Panels on the right are diffraction pattern quadrants obtained at doses of 25 and 50 e/Å^2. The scale bar is 1 nm^{-1}. The dose rate for these diffraction experiments was 0.1 e/Å^{2}s. (d) Radially averaged and background-subtracted diffraction intensities as a function of accumulated dose. Here, the data are vertically shifted for clarity. (e) Integrated intensities of the 002, 020, and 022 diffraction spots, highlighted in (d), showing exponential decay with critical doses of $D_{c,020}$ = 14 e/Å^2, $D_{c,002}$ = 18 e/Å^2, and $D_{c,022}$ = 16 e/Å^2. (f) Lattice parameters of ZIF-L as a function of accumulated electron dose relative to initial lattice parameters (b_0 = 17.11 Å and c_0 = 19.97 Å) determined from 020 and 002 diffraction spot positions.

a_0 = 24.12 Å, b_0 = 17.06 Å, and c_0 = 19.74 Å and has large central pores of dimensions of 9.4 Å × 7.0 Å × 5.3 Å[31] (Figure 1b). This ZIF-L MOF can be synthesized as large uniform flat sheet-like particles,[31] a few μm in length and 100−300 nm in thickness[17,18] with high purity (also see, SI, Figure S1). Figure 1c shows a low-magnification HAADF-STEM image of several ZIF-L particles showing uniform, leaf-like morphology with a longer dimension corresponding to the *b*-axis and the shorter dimension corresponding to the *c*-axis. The particles exhibit a strong diffraction contrast in BF-TEM images visible as bend contours (Figure 1d). When deposited on the holey-carbon TEM grid, they typically land flat on the carbon support of the grid with the [100] zone axis along the incident beam direction and, therefore, allowing direct visualization of the pores in high-resolution (HR) TEM images (Figure 1e). The alternating arrangement of the pores along the *c*-direction, which is specific to the ZIF-L structure, is readily detectable.

https://doi.org/10.1021/acs.chemmater.1c01332
Chem. Mater. 2021, 33, 5681−5689

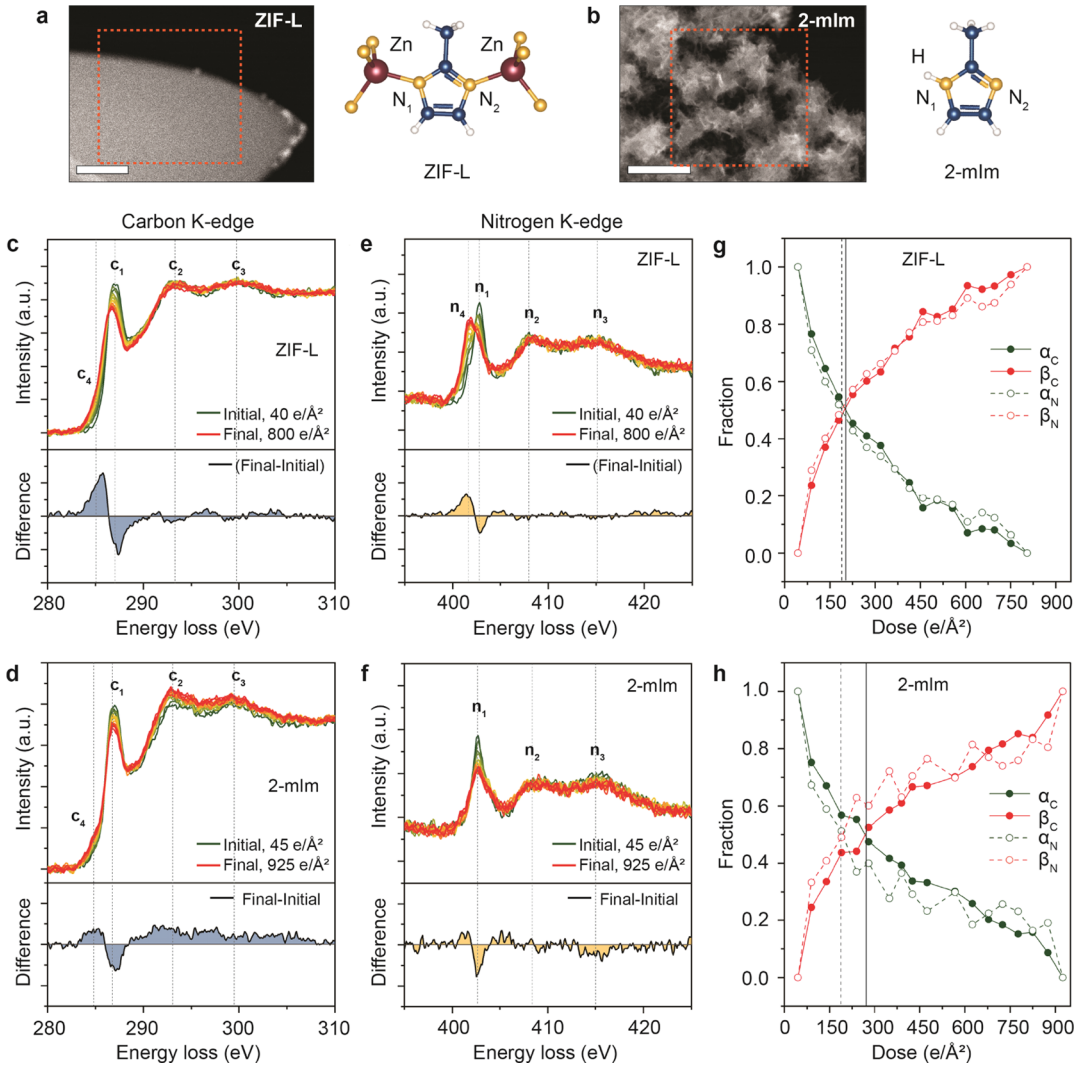

Figure 3. Core-loss EELS from ZIF-L and 2-mIm as a function of dose. (a, b) HAADF-STEM image of ZIF-L and free-standing 2-mIm. The EELS acquisition region over the hole is indicated with the orange boxes. The scale bar is 500 nm. Models of the Zn−(2-mIm) linkage with the two pyrrole-type N atoms and free-standing 2-mIm molecule with the two chemically different N atoms (N_1 for pyrrole-type and N_2 for pyridine-type) are shown on the right. Color codes of the atoms are the same as Figure 1. (c, d) Set of C K-edge spectra from ZIF-L and free-standing 2-mIm for different doses. The identifiable peaks are labeled as c_1, c_2, c_3, and c_4. Difference spectra between initial and final C K-edges are shown in the panel below. (e, f) Set of N K-edge spectra from ZIF-L and free-standing 2-mIm for different doses. The identifiable peaks are labeled as n_1, n_2, n_3, and n_4. Difference spectra between initial and final N K-edges are shown in the panel below. (g, h) Change in C and N K-edges for ZIF-L and free-standing 2-mIm as a function of dose evaluated from linear-regression coefficients: $I(E) = \alpha I^{(i)}(E) + \beta I^{(f)}(E)$, using the initial and final spectra. The solid and dashed vertical lines mark the half points. The dose rate for these EELS measurements was 0.2 e/Å^{2}s. Color code for plots: green (low dose) to red (high dose).

First, changes in the structure and morphology of ZIF-L particles were monitored using BF-TEM and HAADF-STEM imaging. The bend contours visible in individual ZIF-L particles gradually fade away and completely disappear at an accumulated dose of 50 e/Å^2 (Figure 2a) pointing to the loss of crystallinity. At this stage, while there are no obvious visible changes in the particle morphology in HAADF-STEM images (Figure 2b), a few % particle shrinkage along both lateral directions is detectable (see the SI, Figure S2) consistent with an earlier prediction of pore collapse.[32]

To understand the structural changes occurring at these low electron doses, diffraction analysis was performed. Diffraction patterns from the ZIF-L crystal, oriented along the [100] zone axis, were recorded at different electron doses (Figure 2c). A pronounced loss of intensity in the diffraction spots can be observed even at a dose of 25 e/Å^2. To quantify the changes in the electron diffraction patterns, the radially averaged intensities are obtained and evaluated (Figure 2d). A complete loss of the strongest 020 spot intensity occurs at an accumulated dose of 100 e/Å^2, which indicates that the crystallinity of the structure disappears at doses much greater than that indicated by the BF-TEM image analysis. The drop of individual {002} diffraction spot intensities as a function of the dose can be described by an exponential decay, $I = I_0 \exp\{-D/D_c\}$, with critical doses of $D_{c,020}$ = 14 e/Å^2 and $D_{c,002}$ = 18 e/Å^2 (Figure 2e). A similar analysis performed on diffraction patterns obtained with a 300 keV electron beam resulted in slightly higher critical doses, ~26 e/Å^2 (see the SI, Figure S3), indicating that the degradation of the ZIF-L crystal structure could be radiolitic in nature. It should be noted that the decay of diffraction spot intensity depends on the total accumulated electron dose and is relatively insensitive to the

https://doi.org/10.1021/acs.chemmater.1c01332
Chem. Mater. 2021, 33, 5681−5689

dose rate in the range investigated (0.06−0.29 e/Å^{2}s) (see the SI, Figure S3).

In addition to the decrease in spot intensities, shifts in peak positions are also observed for 002, 020, and 022 diffraction spots. The analysis of the shifts for the 020 and 002 spots at an accumulated dose of 50 e/Å^2 indicates about a 2.5% decrease in the lattice parameter b and a 5% decrease for the lattice parameter c (Figure 2f) consistent with the 3 and 6% particle shrinkage along the b- and c-directions, respectively, observed in HAADF-STEM images (see the SI, Figure S2). While changes along the a-direction (beam direction) could not be obtained, a 10% shrinkage along the a-direction for ZIF-L upon electron-beam irradiation was observed by AFM.[18] These results point to a continuous rearrangement of the atomic bonds within the framework and a gradual collapse of the pores. It should be noted that a decrease in lattice parameters and a reduction of the unit cell volume were also observed in X-ray-irradiated ZIF MOFs.[16]

The analysis of radially averaged diffraction intensities also shows the appearance of broad amorphous-like peaks with the decay of diffraction spot intensities (Figure 2d and SI, Figure S3). The first amorphous-like peak appears at a d-spacing of 1.6 nm^{-1} (or 6.2 Å in real space), which matches well to those observed in the pair distribution functions (PDFs) of amorphous ZIFs.[10] Considering that the distance between two neighboring Zn atoms in the ZIF-L framework is d_1 = 6.1 Å,[31] it can be argued that the linker molecules likely determine the first nearest-neighbor distance between metal atoms in disordered ZIF analogous to atomic bond lengths in amorphous inorganic materials. Thus, based on the observations discussed so far, it can be concluded that at this initial stage, when the electron doses are <100 e/Å^2, the pores collapse resulting in the formation of an amorphous-like disordered ZIF phase, which retains the short-range order of the parent ZIF-L crystal.

To understand the changes in the local chemistry in the disordered ZIF-L after exceeding doses of 100 e/Å^2, EELS analysis was performed. Changes in C and N K-edges, which are sensitive to the local bonding environment of the atoms, were evaluated. As before, the data were collected for the 200 keV electron beam by scanning the probe over a region of the sample that was over the hole on the TEM grid (Figure 3a). Electron irradiation doses reaching up to 10^3 e/Å^2 were used in these measurements. For comparison, EELS data were also obtained from free-standing 2-mIm molecules under the same exposure conditions (Figure 3b).

As can be seen from the models in Figure 3, when the 2-mIm molecule is free standing and not part of the MOF, it has two N atoms that are bonded differently: one is a pyrrole-type (N_1) with N bonded to a H atom and its two electrons are part of the π^* system contributing to the aromaticity of the ring; the second is a pyridine-type (N_2) with no bonding to H and its electrons mostly localized in sp^2 orbitals. However, in ZIF-L MOF, both N atoms (N_1 and N_2) of the bridging 2-mIm are linked to the tetrahedrally coordinated Zn metal atoms and have a similar chemical bonding environment, resembling the pyrrole-type N. Unlike N atoms, C atoms in both the free-standing and in linker 2-mIm molecules have very similar bonding environment.

The core-level C K-edge EELS spectra were recorded from both ZIF-L particles and free-standing 2-mIm molecules for doses reaching 800 e/Å^2 (Figure 3c,d, also see the SI, Figures S4 and S5). At low doses (<100 e/Å^2), they show a negligible change in the fine structure, indicating a minimum change in the chemical environment (see the SI, Figure S4). The characteristic energies of three distinct features of the C K-edge, labeled as c_1, c_2, and c_3, corresponding to excitation of electrons from the 1s → 1π^* and 1s → 1σ^* states (there are two types of C σ-bonds in 2-mIm: C−C and C−N) are summarized in Table 1. As the dose increases, the intensity of the peak c_1 (π^* transition) and the sharpness of the peaks c_2 and c_3 (σ^* transitions) decrease (visualized with the difference spectra). These changes indicate that some of the double bonds in the aromatic ring along with reported single bonds in the sp^3-bonded bridging methyl group in 2-mIm are breaking.[34,35] An increase in intensity at energies lower than the π^* peak, labeled as the "shoulder" c_4, is observed in both cases. A likely source for the appearance of this shoulder at 284.6 eV is the opening of the aromatic ring (with very minor contributions from C contamination (see the SI, Figure S6)). Polymerization and formation of some carbon dangling bonds cannot be excluded.[36,37] The difference between changes in C K-edge fine structure in ZIF-L and free-standing 2-mIm is the amount of the π^* peak position shift: from 287.1 to 286.7 eV in ZIF-L, and negligible in free-standing 2-mIm molecules.

Table 1. Summary of Peaks in the Core-Levels EELS of C and N K-Edge Fine Structures for 2-mIm and ZIF-L Along With Those in Imidazole Obtained from Gas-Phase EELS[33]

		2-mIm	ZIF-L	imidazole	transition
carbon	c_1	286.9	286.9	286.7	1s → 1π^*
	c_2	292.5	292.6	292.2	1s → 1σ^*
	c_3	299.0	299.2	298	1s → 1σ^*
	c_4	284.6	284.9		
nitrogen	n_1	402.5(N_1)	402.8	399.9 (N_2)	1s → 1π^*
				402.3 (N_1)	
	n_2	408	408.3	406.8	1s → 1σ^* (C-N_1)
	n_3	415	414.9	415	1s → 1σ^* (C-N_2)
	n_4		401.8		

Core-level EELS spectra of N K-edge from both ZIF-L and 2-mIm were also measured as a function of irradiation dose (Figure 3e,f, also see the SI, Figures S4 and S5). Three main features in N K-edge, labeled as n_1, n_2, and n_3, correspond to the excitation of core electrons from the 1s → π^* and 1s → σ^* states for N with details summarized in Table 1. It should be noted that in free-standing 2-mIm molecules, only a single n_1 peak at 402.5 eV is observed, which corresponds to the 1s → π^* transitions, whereas two peaks have been reported for imidazole structures (see Table 1). This is attributed to the presence of H-bonding in the solid 2-mIm, making the environment of N_2 identical to N_1.[33,38,39] In ZIF-L, as the dose increases, the π^* peak intensity (n_1) decreases and a peak at 401.8 eV (n_4) starts to develop and increase in intensity. This suggests considerable internal structural modifications of the 2-mIm linkers arising from the formation of new C=N bonds due to fragmentation of the aromatic ring or possible polymerization of the 2-mIm molecules.[36,40,41] In free-standing 2-mIm molecules, where N−Zn bonds are absent, only a decrease in the N π^* peak intensity is observed for the same irradiation doses (Figure 3f).

To quantify changes in the C and N K-edge as a function of dose, each spectrum in the set was fitted to a linear superposition of the "initial" and "final" spectra recorded

https://doi.org/10.1021/acs.chemmater.1c01332
Chem. Mater. 2021, 33, 5681−5689

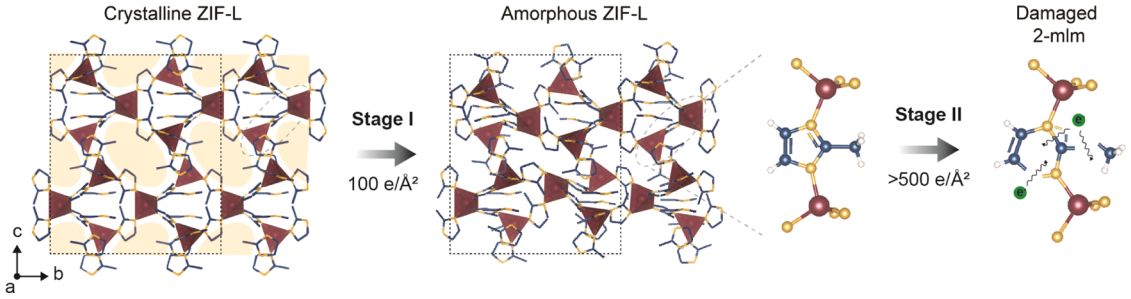

Figure 4. Schematic of changes in ZIF-L at different accumulated electron doses. Crystalline ZIF-L is shown on the far left when viewed along the *a*-direction with the central pores highlighted in yellow. The dotted-line box represents the unit cell of the crystal. Degradation stages: (I) amorphous-like ZIF-L is formed through the collapse of the porous framework at lower electron doses (<100 e/Å^2) with Zn−(2-mIm) bonds still intact; (II) continuous breakdown of the organic 2-mIm linkers at higher electron doses (>100 e/Å^2) while maintaining Zn−N bridging bonds.

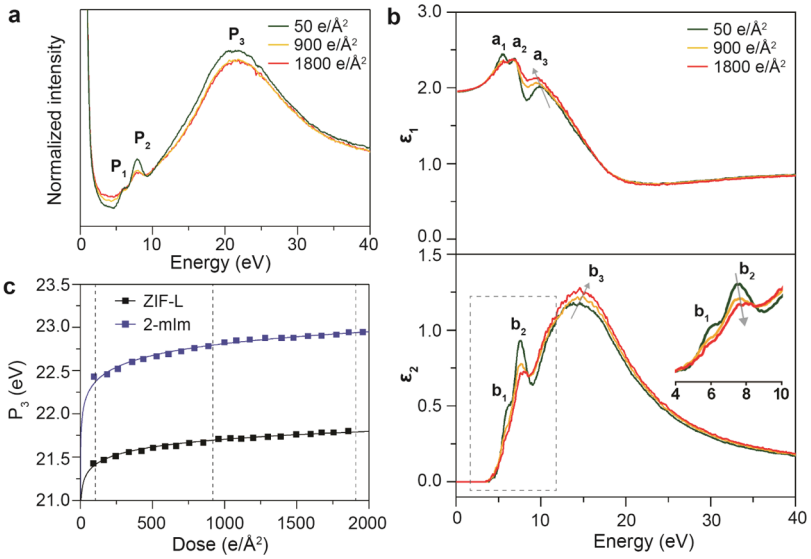

Figure 5. Low-loss EELS and dielectric function of ZIF-L as a function of dose. (a) Low-loss EELS spectra from ZIF-L at three different electron-beam irradiation doses: 50, 900, and 1800 e/Å^2. The spectra are normalized to the zero-loss peak (ZLP). (b) Real, $\varepsilon_1(E)$, and imaginary, $\varepsilon_2(E)$, parts of the complex dielectric function, $\varepsilon(E) = \varepsilon_1(E) + i\varepsilon_2(E)$, obtained from low-loss EELS spectra shown in panel (a) using Kramers−Kronig analysis. Here, refractive index $n = 1.4$ was used.[20,23] The lower-energy region of the dielectric function showing a_1, a_2, and a_3 prominent features in $\varepsilon_1(E)$ and b_1 and b_2 in $\varepsilon_2(E)$ (inset). The shifts in peak positions are indicated by the arrows. (c) Shift of the peak P_3 as a function of accumulated dose. Dashed vertical lines mark doses of 50, 900, and 1800 e/Å^2. The dose rate for these EELS measurements was 1 e/Å^{2}s.

from the sample using linear regression: $I(E) = \alpha I^{(i)}(E) + \beta I^{(f)}(E)$. The results are shown in Figure 3g,h for ZIF-L and 2-mIm, respectively. For ZIF-L, the critical dose at which half of the transformation is reached was $D_{1/2} = 200$ e/Å^2, whereas for free-standing 2-mIm molecules, they were $D_{1/2} = 280$ e/Å^2 and $D_{1/2} = 180$ e/Å^2 for C K-edge and N K-edge, respectively. Additionally, when the integrated intensities of C and N K-edges were evaluated, it was observed that while in both materials the total carbon signal showed a minor reduction, which could result from the loss of the bridging methyl groups of the 2-mIm linker, the nitrogen signal is systematically decreasing in free-standing 2-mIm molecules (see the SI, Figure S7).

These observations indicate that the binding of nitrogen to Zn atoms of the ZIF-L is more stable under electron irradiation. Due to the presence of H, radiolitic modification of the 2-mIm can result in breaking the sp^3-bonded bridging methyl group and ring opening of the imidazole molecules.[25,35,40,42,43] When 2-mIm is present by itself, N atoms in the system can be lost as NH_3 molecules but when bonded to Zn in the ZIF framework, it prevents the removal of N atoms from the structure. Additional measurements of the Zn EELS $L_{2,3}$-edge as a function of dose showed no visible changes (see the SI, Figure S8), further reinforcing this conclusion.

The results discussed above suggest that interactions between the incident beam electrons and ZIF-L MOF are radiolytic-type in nature. To test this further, two new sets of experiments were conducted. In the first set, all of the conditions of the STEM experiment were kept the same, but time (or dose) gaps were introduced into the beam exposure of the sample (see the SI, Figure S9). The results showed that the modifications in ZIF-L due to electron-beam irradiation with and without exposure gaps are very similar, indicating the absence of long beam-sample interaction relaxation times. In the second set, ZIF-L samples were first irradiated by a 5 keV electron beam in a scanning electron microscope (SEM) with different electron doses and then changes in C and N K-edges were evaluated (see the SI, Figure S10). The results showed that on factoring in a 40× difference in the electron-beam energy, the effects of irradiation with 5 keV SEM or 200 keV STEM beam are identical, further supporting the radiolitic-type beam-ZIF-L interaction.[44] It should be noted that these 5

https://doi.org/10.1021/acs.chemmater.1c01332
Chem. Mater. 2021, 33, 5681−5689

keV SEM electron-beam exposure experiments are similar to those used in patterning applications.[17−19]

Observations of (1) changes in C and N K-edge fine structures and no mass loss in disordered ZIF-L and (2) changes in C K-edge and the removal of N atoms in the free-standing 2-mIm molecules under higher electron doses point to the presence of the second stage of structural modifications in ZIF-L. These two stages of the ZIF-L degradation under electron irradiation are schematically illustrated in Figure 4. Electron-beam patterning techniques generally utilize the solubility of either the amorphous or crystalline domains patterned in different solvents such as water and pyridine, respectively.[18,19] Hence, at stage I, after transformation of ZIF-L MOF from crystalline to a disordered structure at lower doses of 100 e/Å^2, the shrinking of the porous structure in the irradiated areas can act as a barrier to solvent penetration, providing enhanced stability against dissolution. This enables patterning of the amorphous MOF phases. Similarly, a complete degradation of the linker structure at Stage II could result in the generation of byproducts, which are more susceptible to dissolution enabling patterning of crystalline MOFs. Thus, the above findings could be used to tailor patterning even further by adjusting the electron dose depending on the incident electron-beam energy.

Further, low-loss EELS was also measured at the same doses as core-level EELS to evaluate the effect of the structural degradation of ZIF-L MOF on the dielectric function, $\varepsilon(E)$, since it dictates the optical properties of the material. Figure 5a shows low-loss spectra for ZIF-L at three accumulated doses: 50, 900, and 1800 e/Å^2, representing the stages of degradation discussed above. Three prominent spectral features in the low-loss EELS, labeled as P_1 to P_3, do modify as the dose increases.

The direct connection between low-loss EELS with Im$\{-1/\varepsilon(E)\}$ and Kramers−Kronig relation allows determination of the real and imaginary parts of the complex dielectric function of the material:[45] $\varepsilon_1(E) = \mathrm{Re}\{\varepsilon(E)\}$ and $\varepsilon_2(E) = \mathrm{Im}\{\varepsilon(E)\}$. The real and imaginary parts of the complex dielectric function of ZIF-L deduced from low-loss spectra are presented in Figure 5b. Two peaks seen in ε_2 (E) at lower energy (b_1 and b_2) correspond to the peaks P_1 (6.2 eV) and P_2 (7.5 eV) seen in the EELS spectra (Figure 5a). These are the lower-energy interband excitations between the $\pi \rightarrow \pi^*$ orbitals in 2-mIm molecules. The broader dominant peak at about 22.5 eV is a combination of collective oscillations as well as higher-energy interband transitions ($(\pi, \sigma) \rightarrow (\pi^*, \sigma^*)$ excitations).[46,47] When the material goes from stage I to stage II with continuous electron irradiation, a decrease in the intensity of b_1 and b_2 is observed, which is a consequence of bonds breaking within 2-mIm. Additionally, the resonances corresponding to the following electronic transitions gradually shift: a_3 in ε_1 (E) lowers its energy and b_2 and b_3 in $\varepsilon_2(E)$ increase it. Particularly noteworthy is the drop in the intensity of peak P_3 and its shift from 21.4 to 22.8 eV (Figure 5c). These changes in dielectrics function are consistent with the gradual degradation of 2-mIm linkers in stage II (also see SI, Figure S11).

CONCLUSIONS

Two distinct stages of structural and chemical changes were identified in ZIF-L MOF when exposed to electron-beam irradiation using a combination of imaging, electron diffraction, and EELS in the TEM. At relatively lower electron doses of <100 e/Å^2, the formation of an amorphous-like disordered ZIF-L phase is detected, which was determined from diffraction pattern analysis and was consistent with previous observations. At this stage, ZIF-L with collapsed pores retains the chemistry of the parent ZIF, which was confirmed from the core-level EELS analysis. At doses above 100 e/Å^2, disordered ZIF-L goes through a second stage of the electron-beam-induced modifications when the internal structure of 2-mIm linker molecules starts to break down. The breaking of the bonds within the organic linker was identified from core-loss EELS C and N K-edge analysis. The low-loss EELS analysis shows that with continuous electron-beam exposure not only 2-mIm linker molecules in disorder ZIF-L continue to break down, but the dielectric function of the material continues to change, shifting the energies for optical transitions important for device applications.

METHODS

Synthesis of ZIF-L and TEM Sample Preparation. ZIF-L was synthesized based on the following procedure:[31] Zinc nitrate hexahydrate (0.59 g, Sigma-Aldrich, 98%) and 1.30 g of 2-methylimidazole (2-mIm) (Sigma-Aldrich, 99%) were separately dissolved in 40 mL of deionized water. The zinc nitrate solution was then added to the 2-mIm solution drop-wise under stirring. The reaction mixture was stirred at room temperature for 4 h. The formed ZIF-L crystals were collected by centrifugation at 1.5×10^4 rpm for 25 min and washed twice with deionized water (10^4 rpm, 15 min). The final product was dispersed in deionized water for the TEM sample preparation. The TEM samples were prepared by drop-casting the ZIF-L suspension on holey-carbon grids (Cu-300HN, Pacific Grid-Tech) and allowed to air dry. For the preparation of free-standing 2-mIm molecules, 2-mIm crystals were suspended in deionized water and sonicated for 2 min. The sample was drop-casted onto the holey-carbon grid and allowed to air dry. All of the TEM samples were stored under a high vacuum (10^{-6} torr) after drying, prior to inserting them into the TEM and, therefore, minimizing their exposure to ambient conditions.

SEM Imaging and Electron-Beam Exposures. Samples for SEM electron-beam exposure were prepared by attaching a TEM grid to an SEM stub using the carbon tape. Electron-beam exposure for different accumulated doses at 5 keV was conducted on an FEI Helios Nanolab G4 dual-beam Focused Ion Beam microscope. Square areas, 3 μm × 3 μm in size, were irradiated with the SEM probe at a probe current of 6−25 pA using 0.5−1 μs/pixel dwell time, and the scan times were adjusted to obtain the desirable accumulated dose.

TEM Imaging, Electron diffraction, and EELS Measurements. HR-TEM imaging and electron diffraction experiments at 300 keV were conducted on an FEI Technai G_2 F30 (S)TEM microscope equipped with a TWIN pole piece and Schottky field emission gun. This microscope is equipped with Gatan 4 k × 4 k Ultrascan CCD and Gatan K2 Summit cameras. Selected area electron diffraction patterns were collected sequentially with an integration time of 2−4 s/frame (2048 px × 2048 px). HR-TEM images were acquired using the K2 camera operated in the counting mode with a dose rate of 0.25 e/Å^{2}s (20 frames (3710 px × 3838 px) with 0.5 s/frame exposure). HR-TEM image simulation was performed using the TEMSIM code, which is based on the Multislice method.[48]

HAADF-STEM imaging, EELS, and electron diffraction measurements at 200 keV were performed on an aberration-corrected FEI Titan 60-300 (S)TEM, which is equipped with a CEOS DCOR probe corrector, monochromator, super-X energy-dispersive X-ray spectrometer, and Gatan Enfinium ER EELS spectrometer. HAADF-STEM images were acquired with a probe convergence angle of 25.5 mrad and the detector inner and outer angles of 55 and 200 mrad, respectively. STEM-EELS measurements were performed using a probe current of 10 pA and a convergence angle of 25.5 mrad with a collection angle of 28 mrad. Spectra were collected by scanning the beam over the regions of interest on the sample, suspended over vacuum, with a dwell time of 1 μs/pixel. Spectra were collected

https://doi.org/10.1021/acs.chemmater.1c01332
Chem. Mater. 2021, 33, 5681−5689

sequentially every 10−20 s in the Dual EELS mode for energy alignment of the core-loss spectra. Energy dispersions of 0.01, 0.025, and 0.05 eV/channel were used for low-loss, and 0.1 and 0.25 eV/channel for core-loss EELS acquisitions. The full-width at half-maxima (FWHM) of the ZLP was 0.6 or 0.8 eV.

Electron Diffraction and EELS Data Analysis. The radially averaged electron diffraction data were fitted to a combination of a power law (for the background) and Gaussian (for the individual diffracted spots and broad peaks) functions of the following form

$$I(x) = ax^b + \sum_{i=1}^{n} c_i e^{-(x-x_{0,i})^2/2\sigma_i^2} + d$$

where a and b are parameters of the power-law fit for the background, c_i and $x_{0,i}$ are intensity and position of the diffraction spot "i" with SD of σ_i, n is the number of spots present, and d is a constant for the dark current of the detector. The fitting parameters were optimized using a nonlinear least-squares solver in MATLAB.

All core-loss EELS spectra were aligned used the ZLP of the dual EELS acquisition. For C K-edge, the background was subtracted using the 265−280 eV energy window in Digital Micrograph. Spectra collected from multiple particles under the identical dose-rate conditions were summed to improve the signal-to-noise ratio of the EELS data sets. Low-loss EELS spectra were all aligned to the ZLP and normalized to the ZLP maxima. To determine the position of the peak P_3, a fourth-order polynomial function was fitted to the spectra in the 15−35 eV energy window and the peak maxima were determined by obtaining the roots of the derivative of the fitted function. For complex dielectric function determination from low-loss EELS, Fourier-log deconvolution was first applied to obtain the single scattering distribution. Then, Kramers−Kronig analysis[49] was performed using MATLAB.

■ ASSOCIATED CONTENT

Supporting Information

The Supporting Information is available free of charge at https://pubs.acs.org/doi/10.1021/acs.chemmater.1c01332.

Lateral size distribution of ZIF-L particles, HAADF-STEM image of ZIF-L particles at different electron doses, electron diffraction of ZIF-L MOF with the 300 keV beam, core-loss EELS fine structure changes in ZIF-L at lower accumulated doses for the 200 keV electron beam, core-loss EELS fine structure changes in ZIF-L at higher accumulated doses for the 200 keV electron beam, estimation of the carbon contamination level in STEM using HAADF image intensity, integrated EELS edge intensity for C and N K-edge for ZIF-L and 2-mIm, Core-loss EELS of the Zn $L_{2,3}$-edge for ZIF-L as a function of dose, comparison of core-loss EELS fine structure changes in ZIF-L under continuous and paused electron-beam exposures, core-loss EELS fine structure changes in ZIF-L under 5 keV STEM electron-beam irradiation, Low-loss EELS changes in ZIF-L and 2-mIm at different irradiation doses (PDF)

■ AUTHOR INFORMATION

Corresponding Author

K. Andre Mkhoyan − *Department of Chemical Engineering and Materials Science, University of Minnesota, Minneapolis, Minnesota 55455, United States;* orcid.org/0000-0003-3568-5452; Email: mkhoyan@umn.edu

Authors

Supriya Ghosh − *Department of Chemical Engineering and Materials Science, University of Minnesota, Minneapolis, Minnesota 55455, United States*

Hwanhui Yun − *Department of Chemical Engineering and Materials Science, University of Minnesota, Minneapolis, Minnesota 55455, United States*

Prashant Kumar − *Department of Chemical Engineering and Materials Science, University of Minnesota, Minneapolis, Minnesota 55455, United States; Department of Chemical Engineering, University of Michigan, Ann Arbor, Michigan 48109, United States;* orcid.org/0000-0003-4622-0917

Sabrina Conrad − *Department of Chemical Engineering and Materials Science, University of Minnesota, Minneapolis, Minnesota 55455, United States*

Michael Tsapatsis − *Department of Chemical Engineering and Materials Science, University of Minnesota, Minneapolis, Minnesota 55455, United States; Department of Chemical and Biomolecular Engineering & Institute for NanoBioTechnology, Johns Hopkins University, Baltimore, Maryland 21218, United States; Applied Physics Laboratory, Johns Hopkins University, Laurel, Maryland 20723, United States;* orcid.org/0000-0001-5610-3525

Complete contact information is available at: https://pubs.acs.org/10.1021/acs.chemmater.1c01332

Author Contributions

S.G., P.K., and K.A.M. conceived and designed the project. S.G. carried out the synthesis, TEM sample preparation, diffraction experiments, SEM, and STEM-EELS experiments. H.Y. assisted with the analysis of the EELS data. S.C. and M.T. assisted with the synthesis. S.G. and K.A.M. prepared the manuscript with contributions from all authors. K.A.M. directed all aspects of the project.

Notes

The authors declare no competing financial interest.

■ ACKNOWLEDGMENTS

This work was supported primarily by the National Science Foundation through the University of Minnesota MRSEC under award numbers DMR-1420013 and DMR-2011401. Parts of this work were carried out in the Characterization Facility, University of Minnesota, which receives partial support from the NSF through the MRSEC and the NNCI (award number ECCS-2025124) programs. The authors thank Dr. Jason C. Myers for help with probe current measurements and TEM assistance.

■ REFERENCES

(1) Furukawa, H.; Cordova, K. E.; O'Keeffe, M.; Yaghi, O. M. The Chemistry and Applications of Metal-Organic Frameworks. *Science* **2013**, *341*, No. 1230444.

(2) Mason, J. A.; Oktawiec, J.; Taylor, M. K.; Hudson, M. R.; Rodriguez, J.; Bachman, J. E.; Gonzalez, M. I.; Cervellino, A.; Guagliardi, A.; Brown, C. M.; Llewellyn, P. L.; Masciocchi, N.; Long, J. R. Methane Storage in Flexible Metal-Organic Frameworks with Intrinsic Thermal Management. *Nature* **2015**, *527*, 357−361.

(3) Phan, A.; Doonan, C. J.; Uribe-Romo, F. J.; Knobler, C. B.; Okeeffe, M.; Yaghi, O. M. Synthesis, Structure, and Carbon Dioxide Capture Properties of Zeolitic Imidazolate Frameworks. *Acc. Chem. Res.* **2010**, *43*, 58−67.

(4) Ma, X.; Kumar, P.; Mittal, N.; Khlyustova, A.; Daoutidis, P.; Mkhoyan, K. A.; Tsapatsis, M. Zeolitic Imidazolate Framework Membranes Made by Ligand-Induced Permselectivation. *Science* **2018**, *361*, 1008−1011.

(5) Li, H.; Wang, K.; Sun, Y.; Lollar, C. T.; Li, J.; Zhou, H. C. Recent Advances in Gas Storage and Separation Using Metal−Organic Frameworks. *Mater. Today* **2018**, *21*, 108−121.

(6) Jiao, L.; Wang, Y.; Jiang, H. L.; Xu, Q. Metal−Organic Frameworks as Platforms for Catalytic Applications. *Adv. Mater.* **2018**, *30*, No. 1703663.
(7) Banerjee, R.; Phan, A.; Wang, B.; Knobler, C.; Furukawa, H.; O'Keeffe, M.; Yaghi, O. M. High-Throughput Synthesis of Zeolitic Imidazolate Frameworks and Application to CO₂ Capture. *Science* **2008**, *319*, 939−943.
(8) Kumar, P.; Kim, D. W.; Rangnekar, N.; Xu, H.; Fetisov, E. O.; Ghosh, S.; Zhang, H.; Xiao, Q.; Shete, M.; Siepmann, J. I.; Dumitrica, T.; McCool, B.; Tsapatsis, M.; Mkhoyan, K. A. One-Dimensional Intergrowths in Two-Dimensional Zeolite Nanosheets and Their Effect on Ultra-Selective Transport. *Nat. Mater.* **2020**, *19*, 443−449.
(9) Gaillac, R.; Pullumbi, P.; Beyer, K. A.; Chapman, K.; Keen, D. A.; Bennett, T. D.; Coudert, F. X. Liquid Metal−Organic Frameworks. *Nat. Mater.* **2017**, *16*, 1149−1155.
(10) Bennett, T. D.; Goodwin, A. L.; Dove, M. T.; Keen, D. A.; Tucker, M. G.; Barney, E. R.; Soper, A. K.; Bithell, E. G.; Tan, J. C.; Cheetham, A. K. Structure and Properties of an Amorphous Metal-Organic Framework. *Phys. Rev. Lett.* **2010**, *104*, 2−5.
(11) Bennett, T. D.; Cheetham, A. K. Amorphous Metal-Organic Frameworks. *Acc. Chem. Res.* **2014**, *47*, 1555−1562.
(12) Cao, S.; Bennett, T. D.; Keen, D. A.; Goodwin, A. L.; Cheetham, A. K. Amorphization of the Prototypical Zeolitic Imidazolate Framework ZIF-8 by Ball-Milling. *Chem. Commun.* **2012**, *48*, 7805−7807.
(13) Bennett, T. D.; Keen, D. A.; Tan, J. C.; Barney, E. R.; Goodwin, A. L.; Cheetham, A. K. Thermal Amorphization of Zeolitic Imidazolate Frameworks. *Angew. Chem. Int. Ed.* **2011**, *50*, 3067−3071.
(14) Henke, S.; Wharmby, M. T.; Kieslich, G.; Hante, I.; Schneemann, A.; Wu, Y.; Daisenberger, D.; Cheetham, A. K. Pore Closure in Zeolitic Imidazolate Frameworks under Mechanical Pressure. *Chem. Sci.* **2018**, *9*, 1654−1660.
(15) Zhou, Y.; Liu, C. J. Amorphization of Metal-Organic Framework MOF-5 by Electrical Discharge. *Plasma Chem. Plasma Process.* **2011**, *31*, 499−506.
(16) Widmer, R. N.; Lampronti, G. I.; Casati, N.; Farsang, S.; Bennett, T. D.; Redfern, S. A. T. X-Ray Radiation-Induced Amorphization of Metal-Organic Frameworks. *Phys. Chem. Chem. Phys.* **2019**, *21*, 12389−12395.
(17) Conrad, S.; Kumar, P.; Xue, F.; Ren, L.; Henning, S.; Xiao, C.; Mkhoyan, K. A.; Tsapatsis, M. Controlling Dissolution and Transformation of Zeolitic Imidazolate Frameworks by Using Electron-Beam-Induced Amorphization. *Angew. Chem. Int. Ed.* **2018**, *57*, 13592−13597.
(18) Miao, Y.; Tsapatsis, M. Electron Beam Patterning of Metal-Organic Frameworks. *Chem. Mater.* **2021**, *33*, 754−760.
(19) Tu, M.; Xia, B.; Kravchenko, D. E.; Tietze, M. L.; Cruz, A. J.; Stassen, I.; Hauffman, T.; Teyssandier, J.; De Feyter, S.; Wang, Z.; Fischer, R. A.; Marmiroli, B.; Amenitsch, H.; Torvisco, A.; Velásquez-Hernández, M.; de, J.; Falcaro, P.; Ameloot, R. Direct X-Ray and Electron-Beam Lithography of Halogenated Zeolitic Imidazolate Frameworks. *Nat. Mater.* **2021**, *20*, 93−99.
(20) Wang, H.; Li, N.; Hu, Z.; Bennett, T. D.; Zhao, X.; Ching, W. Y. Structural, Electronic, and Dielectric Properties of a Large Random Network Model of Amorphous Zeolitic Imidazolate Frameworks and Its Analogues. *J. Am. Ceram. Soc.* **2019**, *102*, 4602−4611.
(21) Krishtab, M.; Stassen, I.; Stassin, T.; Cruz, A. J.; Okudur, O. O.; Armini, S.; Wilson, C.; De Gendt, S.; Ameloot, R. Vapor-Deposited Zeolitic Imidazolate Frameworks as Gap-Filling Ultra-Low-k Dielectrics. *Nat. Commun.* **2019**, *10*, No. 3729.
(22) Stavila, V.; Talin, A. A.; Allendorf, M. D. MOF-Based Electronic and Opto-Electronic Devices. *Chem. Soc. Rev.* **2014**, *43*, 5994−6010.
(23) Ryder, M. R.; Zeng, Z.; Titov, K.; Sun, Y.; Mahdi, E. M.; Flyagina, I.; Bennett, T. D.; Civalleri, B.; Kelley, C. S.; Frogley, M. D.; Cinque, G.; Tan, J. C. Dielectric Properties of Zeolitic Imidazolate Frameworks in the Broad-Band Infrared Regime. *J. Phys. Chem. Lett.* **2018**, *9*, 2678−2684.
(24) Ugurlu, O.; Haus, J.; Gunawan, A. A.; Thomas, M. G.; Maheshwari, S.; Tsapatsis, M.; Mkhoyan, K. A. Radiolysis to Knock-on Damage Transition in Zeolites under Electron Beam Irradiation. *Phys. Rev. B* **2011**, *83*, No. 113408.
(25) Kohl, H.; Reimer, L. Specimen Damage by Electron Irradiation. In *Transmission Electron Microscopy: Physics of Image Formation*; Springer New York: New York, NY, 2008; pp 456−487.
(26) Liu, L.; Zhang, D.; Zhu, Y.; Han, Y. Bulk and Local Structures of Metal−Organic Frameworks Unravelled by High-Resolution Electron Microscopy. *Commun. Chem.* **2020**, *3*, No. 99.
(27) Ahlenhoff, K.; Preischl, C.; Swiderek, P.; Marbach, H. Electron Beam-Induced Surface Activation of Metal-Organic Framework HKUST-1: Unraveling the Underlying Chemistry. *J. Phys. Chem. C* **2018**, *122*, 26658−26670.
(28) Zhang, D.; Zhu, Y.; Liu, L.; Ying, X.; Hsiung, C. E.; Sougrat, R.; Li, K.; Han, Y. Atomic-Resolution Transmission Electron Microscopy of Electron Beam−Sensitive Crystalline Materials. *Science* **2018**, *359*, 675−679.
(29) Liu, Y.; Liu, L.; Chen, X.; Liu, Y.; Han, Y.; Cui, Y. Single-Crystalline Ultrathin 2D Porous Nanosheets of Chiral Metal-Organic Frameworks. *J. Am. Chem. Soc.* **2021**, *143*, 3509−3518.
(30) Wiktor, C.; Meledina, M.; Turner, S.; Lebedev, O. I.; Fischer, R. A. Transmission Electron Microscopy on Metal-Organic Frameworks-a Review. *J. Mater. Chem. A* **2017**, *5*, 14969−14989.
(31) Chen, R.; Yao, J.; Gu, Q.; Smeets, S.; Baerlocher, C.; Gu, H.; Zhu, D.; Morris, W.; Yaghi, O. M.; Wang, H. A Two-Dimensional Zeolitic Imidazolate Framework with a Cushion-Shaped Cavity for CO2 Adsorption. *Chem. Commun.* **2013**, *49*, 9500−9502.
(32) Collins, S. M.; Kepaptsoglou, D. M.; Hou, J.; Ashling, C. W.; Radtke, G.; Bennett, T. D.; Midgley, P. A.; Ramasse, Q. M. Functional Group Mapping by Electron Beam Vibrational Spectroscopy from Nanoscale Volumes. *Nano Lett.* **2020**, *20*, 1272−1279.
(33) Apen, E.; Hitchcock, A. P.; Gland, J. L. Experimental Studies of the Core Excitation of Imidazole, 4,5-Dicyanoimidazole, and s-Triazine. *J. Phys. Chem. A* **1993**, *97*, 6859−6866.
(34) Gadipelli, S.; Travis, W.; Zhou, W.; Guo, Z. A Thermally Derived and Optimized Structure from ZIF-8 with Giant Enhancement in CO2 Uptake. *Energy Environ. Sci.* **2014**, *7*, 2232−2238.
(35) James, J. B.; Lin, Y. S. Kinetics of ZIF-8 Thermal Decomposition in Inert, Oxidizing, and Reducing Environments. *J. Phys. Chem. C* **2016**, *120*, 14015−14026.
(36) Ciliax, B. J.; Kirk, K. L.; Leapman, R. D. Radiation Damage of Fluorinated Organic Compounds Measured by Parallel Electron Energy Loss Spectroscopy. *Ultramicroscopy* **1993**, *48*, 13−25.
(37) Suenaga, K.; Koshino, M. Atom-by-Atom Spectroscopy at Graphene Edge. *Nature* **2010**, *468*, 1088−1090.
(38) Meyer, F.; Blum, M.; Benkert, A.; Hauschild, D.; Jeyachandran, Y. L.; Wilks, R. G.; Yang, W.; Bär, M.; Reinert, F.; Heske, C.; Zharnikov, M.; Weinhardt, L. Site-Specific Electronic Structure of Imidazole and Imidazolium in Aqueous Solutions. *Phys. Chem. Chem. Phys.* **2018**, *20*, 8302−8310.
(39) Lukens, J. T.; Dimucci, I. M.; Kurogi, T.; Mindiola, D. J.; Lancaster, K. M. Scrutinizing Metal-Ligand Covalency and Redox Non-Innocence: Via Nitrogen K-Edge X-Ray Absorption Spectroscopy. *Chem. Sci.* **2019**, *10*, 5044−5055.
(40) Meißner, R.; Feketeová, L.; Ribar, A.; Fink, K.; Limão-Vieira, P.; Denifl, S. Electron Ionization of Imidazole and Its Derivative 2-Nitroimidazole. *J. Am. Soc. Mass Spectrom.* **2019**, *30*, 2678−2691.
(41) Wang, H. L.; O'Malley, R. M.; Fernandez, J. E. Electrochemical and Chemical Polymerization of Imidazole and Some of Its Derivatives. *Macromolecules* **1994**, *27*, 893−901.
(42) Schmiers, H.; Friebel, J.; Streubel, P.; Hesse, R.; Köpsel, R. Change of Chemical Bonding of Nitrogen of Polymeric N-Heterocyclic Compounds during Pyrolysis. *Carbon* **1999**, *37*, 1965−1978.
(43) Schnabl, H. Does Removal of Hydrogen Change the Electron Energy-Loss Spectra of DNA Bases? *Ultramicroscopy* **1980**, *5*, 147−151.

https://doi.org/10.1021/acs.chemmater.1c01332
Chem. Mater. 2021, 33, 5681−5689

(44) Egerton, R. F.; Li, P.; Malac, M. Radiation Damage in the TEM and SEM. *Micron* **2004**, *35*, 399−409.
(45) Mkhoyan, K. A.; Babinec, T.; Maccagnano, S. E.; Kirkland, E. J.; Silcox, J. Separation of Bulk and Surface-Losses in Low-Loss EELS Measurements in STEM. *Ultramicroscopy* **2007**, *107*, 345−355.
(46) Isaacson, M. Interaction of 25 Kev Electrons with the Nucleic Acid Bases, Adenine, Thymine, and Uracil. i. Outer Shell Excitation. *J. Chem. Phys.* **1972**, *56*, 1803−1812.
(47) Williams, M. W.; Hamm, R. N.; Arakawa, E. T.; Painter, L. R.; Birkhoff, R. D. Collective Electron Effects in Molecular Liquids. *Int. J. Radiat. Phys. Chem.* **1975**, *7*, 95−108.
(48) Kirkland, E. J. *Advanced Computing in Electron Microscopy*, 2nd ed.; Springer: Boston, 2010.
(49) Egerton, R. F. *Electron Energy-Loss Spectroscopy in the Electron Microscope*, 3rd ed.; Springer: Boston, 2011.

https://doi.org/10.1021/acs.chemmater.1c01332
Chem. Mater. 2021, 33, 5681−5689